RSC Advances

PAPER

View Article Online
View Journal | View Issue

Cite this: *RSC Adv.*, 2017, **7**, 19391

Synthesis of magnetic core–shell Fe_3O_4@TiO_2 nanoparticles from electric arc furnace dust for photocatalytic degradation of steel mill wastewater

Saeid Salamat, Habibollah Younesi * and Nader Bahramifar

The study was undertaken to design magnetic core–shell Fe_3O_4@TiO_2 nanoparticles from electric arc furnace dust and evaluate its photocatalytic activity on organic pollutant degradation from steel industry wastewater. Different molar ratios of Fe_3O_4 to TiO_2 were tested on Fe_3O_4@TiO_2 nanoparticles. The materials were characterized using X-ray diffraction, X-ray photoelectron spectroscopy, Fourier transform-infrared spectroscopy, scanning electron microscopy, energy-dispersive X-ray spectroscopy, and transmission electron microscopy, and a zeta potential analyzer and vibrating sample magnetometer. The behavior of Fe_3O_4@TiO_2 nanoparticles under different molar ratios of Fe_3O_4 to TiO_2, pH, photocatalyst dose and temperature was investigated. The apparent rate constant of organic pollutant degradation using Fe_3O_4@TiO_2 was found to be pH dependent as it influenced the surface properties and therefore the photocatalytic activity of Fe_3O_4@TiO_2, which was higher under acidic condition. The degradation of organic pollutants was as high as 96% at pH 3, 1 g L^{-1} photocatalyst dose, 30 °C temperature, after 90 min reaction time, and the apparent rate constant was 0.043 min^{-1}. The thermodynamic parameters of activation, estimated by the Eyring equation and based on transition state theory (TST), indicated a nonspontaneous process in nature with positive $\Delta^{\ddagger}G^{\circ}$ values, an endothermic reaction with positive $\Delta^{\ddagger}H^{\circ}$ and negative $\Delta^{\ddagger}S^{\circ}$ values. High degradation rate and catalyst recovery were maintained after five consecutive recycling cycles.

Received 28th January 2017
Accepted 27th March 2017

DOI: 10.1039/c7ra01238a

rsc.li/rsc-advances

1. Introduction

Khouzestan steel company (KSC) is an iron and steel producer in the south west of Iran, established in 1973 and built on 3.8 km^2 in the vicinity of Ahwaz city. KSC is operated based on a direct reduction method and uses electric arc furnace (EAF) technology, which has an actual capacity of up to 3.6 million tons per year. KSC consumes 8 m^3 of water to produce a tonne of steel. The effluent of steel mill wastewater is transferred into pumping stations through gravity lines. At a predetermined point, the wastewater is pumped through a pressurized force main gravity pipe system that carries the wastewater to the wastewater treatment plant. However, an unfavorable event involving a common issue that impedes with the operation of pumping stations is the accumulation of fat, oil and grease (FOG), which may cause blockages, leading to wastewater spills and backups. Besides, EAF in KSC generate a considerable amount of undesirable wasting metals in the form of a fine dust (*i.e.*, EAF dust) during the melting process.[1] Compared to other wastes, it is difficult to pile up in the open space or landfill as it creates serious environmental problems. In KSC, six arc furnaces are assessed to generate about 60 000 tons of EAF dust per year during the annual steel production of the aforementioned and approximated in the diameter range of 20–25 μm size of particles. The United States environmental protection agency (US EPA) in 1980 categorized the EAF dust as a hazardous industrial waste, due to its chemical and physical properties.[2] In general, disposal or recycling of these heavy metals from EAF is actually quite expensive and inefficient.[3] A previous study suggested that the most abundant elements in EAF dust were iron and some transitional metals.[4] In view of the above, it would be attractive to supply a process for the recovery of iron EAF dust by way of waste prevention and metal values that does not present a difficult solid/liquid extraction system and to cover an alternative application method of treatment and disposal of effluents of steel industries.

Among the oxidation methods, advanced oxidation processes (AOPs) are of great attention for the treatment of those wastewaters with high chemical strength and low biodegradability by conventional methods, due to their thermodynamic feasibility and high oxidative capability for the removal of organic pollutants of wastewater *via* precipitation of free radicals, mainly hydroxyl radicals ($^{\bullet}OH$).[5,6] AOPs can be categorized as homogeneous (Fenton, Fenton-like, O_3/H_2O_2, UV/O_3) and heterogeneous (ZnO/UV, TiO_2/UV and others) processes in which highly reactive hydroxyl radicals are generated, with or without UV irradiation, to attack a great variety of organic compounds.[7,8] Among the wide applied AOPs, TiO_2 is the most

Department of Environmental Science, Faculty of Natural Resources, Tarbiat Modares University, P.O. Box 64414-356, Noor, Iran. E-mail: hunesi@modares.ac.ir; hunesi@yahoo.com; Fax: +98-11-44553499; Tel: +98-11-44553101-3

used semiconductor for removing organic pollutants from the aqueous phase in heterogeneous process. It is well established that TiO_2 with a wide band gap (3.2 eV) and proper UV radiation wavelength ($\lambda < 385$ nm) can generate electron/hole pairs (e^-/h^+) that recombine a conduction band electron and a valence band hole to be able to interact with adsorbed electron acceptors and oxidize electron donors.[9] This catalyst elucidates efficient photocatalytic activity, strong oxidizing power, good chemical and optical stability, non-toxic and at a relatively low cost and long-term stability against photocorrosion and chemical corrosion.[10,11] To address the current complications of conventional TiO_2 catalysts as applied in practice, the main weakness of this process is the difficulty in removing the suspension photocatalyst from the treated wastewater at the outlet of the photocatalytic reactor[12,13] and separating such nanoparticles from large volumes of water involves additional cost. To overcome separation problem, immobilization of TiO_2 particles onto support materials (such as quartz, silica gel, alumina, zeolites, activated carbon, glass sphere *etc.*) provides loss of photocatalytic activity, low surface areas, low mass transfer limitation, and difficult to recover and reuse from the photoreactor.[14] Consequently, there is a great demand for ways to improve TiO_2 particles stability and reusability. Potential application of magnetic photocatalyst separation provides a suitable approach for removing and reusing magnetic nanoparticles by applying an appropriate external magnetic field. Using this approach, the agglomeration of the heterogeneous photocatalyst particles can be prevented in the recovery stage and the long-term durability of the photocatalysts may be improved. At present, this is the main technical disadvantages that associated with the application of the photocatalytic wastewater treatment processes.[15] Furthermore, the author has previously reported that the cost associated with a downstream separator may be reduced or may even eliminate a downstream separating unit for a large-scale energy, developing energy-saving technologies.[16] Consequently, TiO_2 photocatalyst has been coated onto the surface of several magnetic supports, for instance polymers,[17] carbon,[18] and silica,[19] zeolite[20,21] and other nanocomposites combining silica mesoporous structure materials with a high surface area and tunable pore size (2–50 nm) with magnetic nanoparticles[22] in order to enhance the photocatalytic ability of nanostructured TiO_2. Xin *et al.*[23] have fabricated a separable Fe_3O_4@TiO_2 core–shell nanocomposite for photocatalytic degradation of Rhodamine B (RhB) solution. Wang *et al.*[24] have recently reported a separable Fe_3O_4@SiO_2@mTiO_2 core–shell nanocomposite and an outer mesoporous TiO_2 (mTiO_2) as the active layer for photocatalytic degradation of methylene blue (MB) solution. However, the major disadvantages of the aforementioned research studies are the relatively high cost of the iron salts (chloride and nitrate salts) and the release of large amounts of chloride and nitrate from iron chloride or iron nitrate, which adds additional cost to the process and would have deleterious to the environment. Therefore, a process to use iron-based EAF dust to produce magnetic photocatalyst compensate the above mentioned cost advantage.

Alongside the above background, for the first time, magnetic core–shell Fe_3O_4@TiO_2 nanoparticles were designed through the preparation of magnetic core Fe_3O_4 nanoparticles from an electric arc furnace dust from the steelmaking industry and TiO_2 shell, so the resulting nanoparticles could be easily separated from treated wastewater under the application of an external magnetic field. The characteristics of photocatalyst were analyzed by several techniques and the UV-light catalytic activity of the resulting nanoparticles was evaluated for the efficiency in the degradation of steel mill wastewater, which showed a low biodegradability, posing serious threats to the environment once released into natural water. The effects of different Fe_3O_4 to TiO_2 ratio, solution pH value, Fe_3O_4@TiO_2 dose and temperature on COD removal were investigated. The recycling capability and reuse of the Fe_3O_4@TiO_2 nanoparticles were also studied. The Langmuir–Hinshelwood was applied to explain the kinetics of the photodegradation of organic pollutant of steel mill wastewater and the thermodynamic parameters of the photocatalytic reaction at various temperatures estimated by the Eyring equation based on the transition state theory.

2. Materials and methods

2.1. Materials

EAF dust, ethylene glycol (EG), sodium acetate anhydrous (CH_3COONa, AcNa), tetraethylorthotitanate (TEOT), tetra-*n*-butylammonium hydroxide (TBAOH) and absolute ethanol were obtained from Merck. All these reagents were used as received without further purification.

2.2. Preparation of Fe_3O_4 nanoparticles

The magnetic particles were synthesized through a solvothermal method Zhao *et al.*[25] with some modification. Table 1 shows the dry composition of EAF dust collected from KSC. The main components are 30.18% total Fe, 13.17% CaO and 7.90% Na_2O, indicating that fine dust contains significantly larger amounts of iron. In a typical procedure, 10 g EAF dust was dissolved by HCl (4 mol) under vigorous stirring for 60 min. The solution was placed in a boiling water-bath for 60 min, and added ethylene glycol (40 mL) to form a clear solution and then

Table 1 Analysis of elemental composition of EAF dust and Fe_3O_4 nanoparticles

	Value ± SD, wt%	
Element	EAF dust	Fe_3O_4 nanoparticles
Total Fe	30.18 ± 5.09	—
FeO	6.26 ± 2.58	—
Fe_2O_3	27.24 ± 5.27	55.45 ± 3.48
SiO_2	1.81 ± 0.30	16.83 ± 1.83
Al_2O_3	0.36 ± 0.14	3.162 ± 0.85
CaO	13.17 ± 3.06	3.427 ± 1.01
MgO	1.56 ± 0.59	1.92 ± 0.73
Na_2O	7.90 ± 3.30	0.29 ± 0.08
K_2O	6.985 ± 0.26	0.172 ± 0.04
SO_3	0.26 ± 0.09	—
P_2O_5	0.22 ± 0.05	3.765 ± 1.03
L.O.I	21.03 ± 1.15	9.6 ± 1.94

sodium acetate (2.0 g) added to the solution at 60 °C under vigorous stirring for 60 min. The mixture was put into a Teflon-lined stainless-steel autoclave (50 mL), thereafter the autoclave was heated at 200 °C for 8 h in an oven and allowed to cool to room temperature. The black particles were collected with the help of a magnet, followed by washing with ethanol and deionized water several times, and then dried under vacuum at 60 °C overnight for further use.

2.3. Preparation of Fe_3O_4@TiO_2 nanoparticles

In preparation of Fe_3O_4@TiO_2, 5 mL of absolute ethanol was mixed with 5 mL of tetrabutylammonium hydroxide and stirred for 1 h by the magnetic stirrer. Then, 5.56 mL of tetraethylorthotitanate and 30 mL diluted water were added. Mixing was continued under heating conditions at 80 °C. After 1 h, 1 g of Fe_3O_4 nanoparticle powder was added to the obtained white gel and was mixed for another 1 h. All the processes were conducted in a Teflon vessel and the mixture was then put in a stainless steel reactor that was kept at 180 °C for 4 days in an oven. The suspension was dried at 25 °C and then calcined at 400 °C for 3 h.

Similarly, we also prepared Fe_3O_4@TiO_2 nanocomposites with ratios of 1 : 0.25, 1 : 0.5, 1 : 1 and 1 : 2 of Fe_3O_4 to TiO_2 and are denoted as FT0.25, FT0.5, FT1 and FT2, respectively.

2.4. Characterization

The elemental composition of EAF dust was determined by X-ray fluorescence (XRF, Philips, Spectrometer PW2404). The crystal structure of Fe_3O_4 and Fe_3O_4@TiO_2 nanoparticles was examined by a Philips XPert MPD X-ray diffraction (XRD), using a Cu Kα radiation ($\lambda = 1.54056$ Å) in the range of 10–90° (2θ) at 40 kV and 30 mA. The Fourier transform infrared (FT-IR) spectra of Fe_3O_4 and Fe_3O_4@TiO_2 were analyzed using the FT-IR spectrometer (Thermo Nicolet 360-FT-IR). The zeta potential of dispersed Fe_3O_4@TiO_2 was determined using a Zetasizer (Ver. 7.11, Malvern Instruments, UK) at room temperature. The measurements were performed with photocatalyst particles at a solid load of 0.1 wt%. Five suspensions with a pH of 2, 4, 6, 8 and 10 were prepared by adding either HCl 0.1 M or NaOH 0.1 M. The size and morphology of the as-synthesized particles were determined by a scanning electron microscope (SEM, KYKY-EM3200). The particle morphology was examined by a transmission electron microscope TEM (Philips CM120, 120 kV). The magnetization and hysteresis loop were measured in air at room temperature with a vibrating sample magnetometer (VSM, Lake shore, 7410). Chemical oxygen demand (COD) was determined for the SMW using a photometric analyzer (DR5000 spectrophotometer, Hach, Germany). X-ray photoelectron spectroscopy (XPS) analysis was employed by Specs model EA10 plus (Bestec Co, Germany) using the Kα line energies of aluminium (AlKα = 1486/6 eV) as a radiation source and ultra-high vacuum (UHV) chamber at a pressure of 10^{-9} Torr.

2.5. Wastewater characteristic

The steel industry wastewater was collected from the pumping stations of mill effluent sumps, the Khouzestan steel company (KSC), southwest of Iran. The wastewater was stored at 4 °C. The characteristics of wastewater, including the chemical oxygen demand (COD), biological oxygen demand (BOD), total suspended solids and turbidity were determined according to standard methods for the examination of water and wastewater[26] as summarized in Table 2.

2.6. Photocatalytic experiments

Photodegradation experiments were carried out in a batch reactor. The cylindrical reactor of 1000 mL capacity was used by taking of 500 mL wastewater containing a certain amount of photocatalyst. Prior to the irradiation, the reaction mixture was purged with oxygen gas for 30 min to perform the reaction under dark condition. Photocatalytic removal efficiency of COD was evaluated to measure the optimum TiO_2 content of the photocatalyst for enhancing the photocatalytic activity of Fe_3O_4@TiO_2 while maintaining constant conditions of reaction temperature, dosage and pH. The Fe_3O_4@TiO_2 photocatalyst at the desired dosage was then used to degrade COD under different pH conditions (3, 4, 5, 6, 7 and 8) in order to verify the effect of pH on photocatalytic activity while maintaining constant conditions of reaction temperature and dosage. A low-pressure mercury vapor lamp (Philips, 9 W, Nederlands) placed in axial position inside a quartz sleeve was used as UV irradiation source. The photocatalytic removal efficiency of COD using Fe_3O_4@TiO_2 nanoparticles was computed by:

$$\text{Photocatalytic removal efficiency} = \frac{\text{COD}_\text{o} - \text{COD}_t}{\text{COD}_\text{o}} \times 100 \quad (1)$$

2.7. Photocatalytic degradation kinetics

The Langmuir–Hinshelwood (L–H) model was applied to describe the initial rate of the photodegradation kinetics of the COD of SMW.

$$r_\text{o} = -\frac{\text{d}C_\text{COD}}{\text{d}t} = \frac{k_\text{r} K C_\text{COD}}{1 + K C_\text{COD}} \quad (2)$$

Table 2 The physicochemical characteristics of SMW

Characteristics	Average values ± SD
pH	7.6 ± 0.2
Total COD, mg L^{-1}	1115.0 ± 107
Soluble COD, mg L^{-1}	558.0 ± 62
Total BOD, mg L^{-1}	550.0 ± 125
Oil and grease, mg L^{-1}	21.8 ± 650
Total solids (TS), mg L^{-1}	201.7 ± 37
Total dissolved solids (TDS), mg L^{-1}	1001.7 ± 80
Total suspended solids (TSS), mg L^{-1}	106.0 ± 10
Fixed suspended solids (FSS), mg L^{-1}	51.3 ± 9.07
Volatile suspended solids (VSS), mg L^{-1}	28.67 ± 6.81
Cl, mg L^{-1}	9.9 ± 0.59
NO_3–N, mg L^{-1}	0.345 ± 0.102
TKN, mg L^{-1}	34.9 ± 4.18
EC, μs cm^{-1}	1808.0 ± 137
DO, mg L^{-1}	6.1 ± 0.404
Turbidity, NTU	70.0

where, where r_o is the initial rate of the disappearance of the COD concentration, C_{COD} the equilibrium bulk-solute concentration and t the reaction time, K the equilibrium constant for adsorption of COD onto the photocatalyst surface and k_r the limiting rate constant of the reaction at maximum coverage under the given experimental conditions. In the case of highly diluted solution, the term KC becomes less than 1, when the denominator of eqn (2) neglected and the reaction rate can be modelled by the apparent first-order kinetics as in the following equation:

$$r = -\frac{dC_{COD}}{dt} = k_r K C_{COD} = k_{app} C_{COD} \quad (3)$$

where, k_{app} the apparent first-order rate constant. The solution to differential eqn (3) with the boundary condition $C = C_o$ at $t = 0$ is:

$$\frac{COD_t}{COD_o} = e^{-k_{app} t} \quad (4)$$

where, COD_o and COD_t are the COD concentration at the initial time ($t = 0$) and any time t ($t = t$), respectively. Thus, by plotting COD_t/COD_o against t, the apparent rate constant can be computed from the nonlinear regression analysis.

2.8. Thermodynamic study

The reaction rate constant and removal efficiency increases with increasing the reaction temperature for Fe_3O_4@TiO_2 photocatalyst decomposition. The activation energy, which is a minimum energy needed for the reaction to occur, can be expressed by the Arrhenius equation:

$$k_{app} = A\, e^{-\frac{E_a}{RT}} \quad (5)$$

where k_{app} is the apparent rate constant for the first order reaction (min^{-1}), A the frequency factor (min^{-1}), E_a the activation energy (kJ mol^{-1}) R the ideal gas constant which is equal to 8.314 J K^{-1} mol^{-1} and T the temperature (K). The linear form of logarithm of eqn (5) can be written as:

$$\ln k_{app} = \ln A - \frac{E_a}{RT} \quad (6)$$

According to transition state theory (TST), the Henry Eyring equation can be used to deduce the temperature dependence of apparent rate constant:[21]

$$k_{app} = \frac{K_B T}{h} \exp\left(-\frac{\Delta^{\ddagger} G^o}{RT}\right) \quad (7)$$

where, K_B is the Boltzmann's constant which is equal to 1.3805×10^{-23} J K^{-1}, h is Planck's constant which is equal to 6.6261×10^{-34} J s and $\Delta^{\ddagger}G^o$ the standard Gibbs free energy change of activation (kJ mol^{-1}). In the thermodynamic property of TST, the standard enthalpy change of activation ($\Delta^{\ddagger}H^o$) and the standard entropy change of activation ($\Delta^{\ddagger}S^o$) are brought together with the change in the standard Gibbs free energy of activation equation:

$$\Delta^{\ddagger} G^o = \Delta^{\ddagger} H^o - T\Delta^{\ddagger} S^o \quad (8)$$

Substitution of eqn (8) into eqn (7) gives:

$$k_{app} = \frac{K_B T}{h} \exp\left(\frac{\Delta^{\ddagger} S^o}{R}\right) \exp\left(-\frac{\Delta^{\ddagger} H^o}{RT}\right) \quad (9)$$

The linear form of the Eyring's equation can be expressed as follows:

$$\ln\left(\frac{k_{app} h}{K_B T}\right) = \frac{\Delta^{\ddagger} S^o}{R} - \frac{\Delta^{\ddagger} H^o}{RT} \quad (10)$$

Therefore a plot of dimensionless values of $\ln(k_{app}h/K_BT)$ against $1/T$ provides a straight line and $\Delta^{\ddagger}H^o$ and $\Delta^{\ddagger}S^o$ are obtained from the slope and the intercept, respectively. According to our previous publication, the following expressions give an additional method of estimating the frequency factor and activation energy can be computed:[21]

$$A = \frac{K_B T}{h} \exp\left(\frac{\Delta^{\ddagger} S^o}{R}\right) \quad (11)$$

$$E_a = \Delta^{\ddagger} H^o + RT \quad (12)$$

3. Result and discussion

3.1. Photocatalyst characterization

3.1.1. XRD analysis. Fig. 1 shows the XRD spectra pattern of TiO_2, Fe_3O_4 and Fe_3O_4@TiO_2 core–shell nanoparticles. The diffraction peak in Fig. 1a shows the XRD pattern of the as-synthesized TiO_2 particles and was found to associate to anatase of TiO_2 (JCPDS no. 21-1272). The observed diffraction peaks in Fig. 1b can be indexed well with relative intensities of standard Fe_3O_4 (JCPDS no. 19-629) indicating that the as-synthesized nanoparticles are the pure Fe_3O_4 phase and single-phase of the face-centered-cubic spinel. By comparing Fig. 1a and b, it is found that the XRD diffraction peak intensities of Fe_3O_4 decreased due to TiO_2 coating. In addition, beside the crystal structure of Fe_3O_4 lies in Fe_3O_4@TiO_2 core–shell nanoparticles, the crystal structure of Fe_3O_4 core–shell nanoparticles is as that of TiO_2 nanoparticles, which is anatase and proves that dissolving Fe^{3+} from Fe_3O_4 seeds in the preparation process does not cause the change of crystal structure. The crystallite or 0.1317 of anatase TiO_2 and Fe_3O_4 were estimated from the corresponding XRD peaks at $2\theta = 25.42$ and 35.50°, respectively, by Scherrer's equation:

$$D = \frac{hk\lambda}{\beta \cos\theta} \quad (13)$$

where D is the crystallite size (nm), λ the wavelength of the X-ray radiation (Cu Kα = 0.1541874 nm), k the Scherrer constant (0.89), β the full width at the half-maximum of the (101) plane of anatase TiO_2 and the (311) plane of Fe_3O_4 and θ the diffraction angle. The crystallite sizes of about 29.7 and 11.6 nm in pure anatase TiO_2 nanoparticles and in Fe_3O_4@TiO_2 nanocomposite and 15.64 and 32.66 nm for Fe_3O_4 nanoparticles and Fe_3O_4 in Fe_3O_4@TiO_2 nanocomposite, respectively, were obtained.

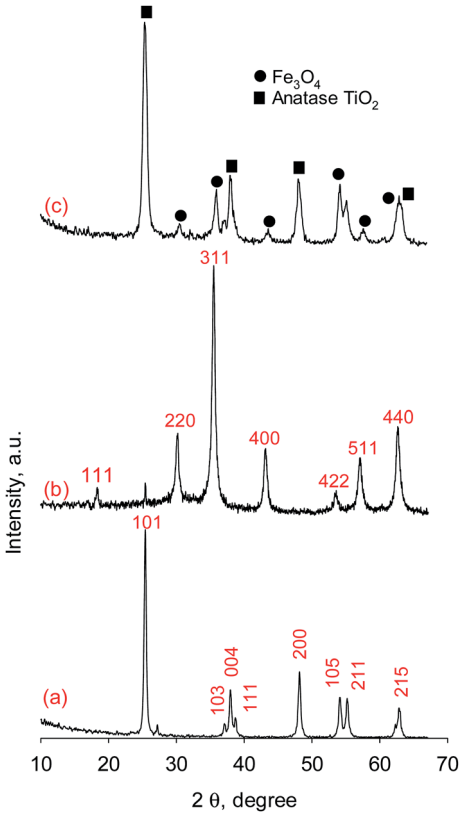

Fig. 1 XRD patterns of (a) anatase TiO_2, (b) Fe_3O_4, and (c) Fe_3O_4@TiO_2.

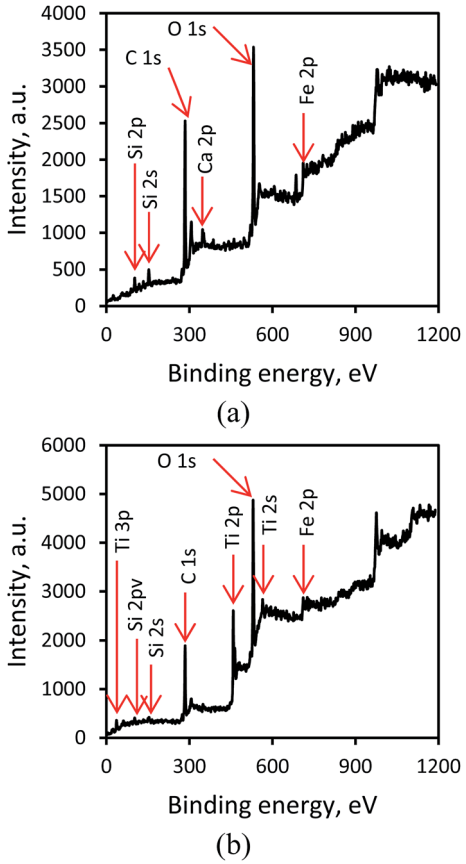

Fig. 2 Wide range XPS spectra of (a) Fe_3O_4 and (b) Fe_3O_4@TiO_2.

3.1.2. XPS analysis. X-ray photoelectron spectroscopy (XPS) analysis was employed to find stoichiometry and surface chemical composition of Fe_3O_4 and Fe_3O_4@TiO_2, as shown in Fig. 2a and b. Fig. 2a shows a total XPS spectrum that composed mainly of two peaks of carbon (C 1s 284.6 eV) and oxygen (O 1s 531.4 eV), deriving from the acetate coating on the surface and remaining carbon from EAF dust (Table 1), silicon (Si 2s 102.2 eV), silicon (Si 2p 153), calcium (Ca 2p 347.4 eV), and Fe (Fe 2p 685.4 eV), related to the oxidized surface of Fe_3O_4, while Fig. 2b shows a strong peak at 459.6 eV is assigned to the Ti 2p and another two weak peaks at the 39.4 and 564.3 eV are assigned to the Ti 3p and the Ti 2s, respectively, as well as a weak peak at a binding energy of about 61.8 eV is attributed to Fe 3p from Fe_3O_4@TiO_2. Fig. 3a and b show the 2p electron orbit of Fe atoms in Fe_3O_4 and Fe_3O_4@TiO_2 nanoparticles, indicating the peaks of Fe $2p_{1/2}$ and Fe $2p_{3/2}$ core-level electrons for the both Fe_3O_4 and Fe_3O_4@TiO_2 samples that are located at a binding energy of 724 and 710.8 eV. According to quantum theory, the degeneracy energy level corresponding to each value of quantum number J is $(2J + 1)$.[27] As can be seen from Fig. 3a and b, of the two peaks, Fe $2p_{3/2}$ peak is more intense than Fe $2p_{1/2}$ peak, and the peak area ratio of Fe $2p_{3/2}$ to Fe $2p_{1/2}$ core level photoelectron of 2 to 1 is observed. This splinting energy of the XPS peaks (ΔE) was found to be 14.6 eV. Furthermore, the narrower and the larger peak area of Fe $2p_{3/2}$ than Fe $2p_{1/2}$ peak is due to spin orbit (J–J) coupling. In addition, it is observed that Fe $2p_{3/2}$ and Fe $2p_{1/2}$ peaks for Fe_3O_4 nanoparticles have two satellite peaks as presented in Fig. 3. The two satellite peaks are located at 728.6 and 715.2 eV, which could also be corresponded to the oxidation state of Fe^{2+}. However, the peaks of Fe 2p for the two samples are located at the same positions. While in the Fe 3p spectra of Fe_3O_4 and Fe_3O_4@TiO_2 nanoparticles, two peaks at 726.4 and 712.8 eV attributing to the binding energies of Fe $2p_{1/2}$ and Fe $2p_{3/2}$, respectively, which is the characteristic of Fe^{3+} in iron oxide nanoparticles. While in the Fe_3O_4@TiO_2 nanoparticles, the peak positions of Fe 3p locates at the same binding energies as compared to Fe_3O_4. The positions of the satellite peaks for the Fe $3p_{1/2}$ and Fe $3p_{3/2}$ are centered at 729.8 and 720.6 eV in Fe_3O_4, respectively, which are assigned to the oxidation state of Fe^{3+} in Fe_3O_4 nanoparticles. Compared with Fe_3O_4, the binding energy of the satellite peaks for the Fe $3p_{1/2}$ and Fe $3p_{3/2}$ of Fe_3O_4@TiO_2 nanocomposites exhibits a negative shift (~1.5 eV) and a positive shift (~0.2 eV), respectively. The XPS results confirm the formation of two compounds of magnetite and the results in the present study were consistent with previous findings.[28]

The XPS spectrum of the Ti 2p for the Fe_3O_4@TiO_2 photocatalyst is shown in Fig. 3c. The surface chemical composition in the nanoparticle photocatalyst showed that the Ti 2p peak involves four different peaks corresponding to two chemical states from doublet consisting of the Ti $2p_{3/2}$ and the Ti $2p_{1/2}$ occurred at binding energies of 457 and 463.1 eV (Ti^{3+}) 458.8 and 464.6 eV (Ti^{4+}), which designates the valences of Ti in the synthesized photocatalyst are +3 and +4. Clearly, the presence of

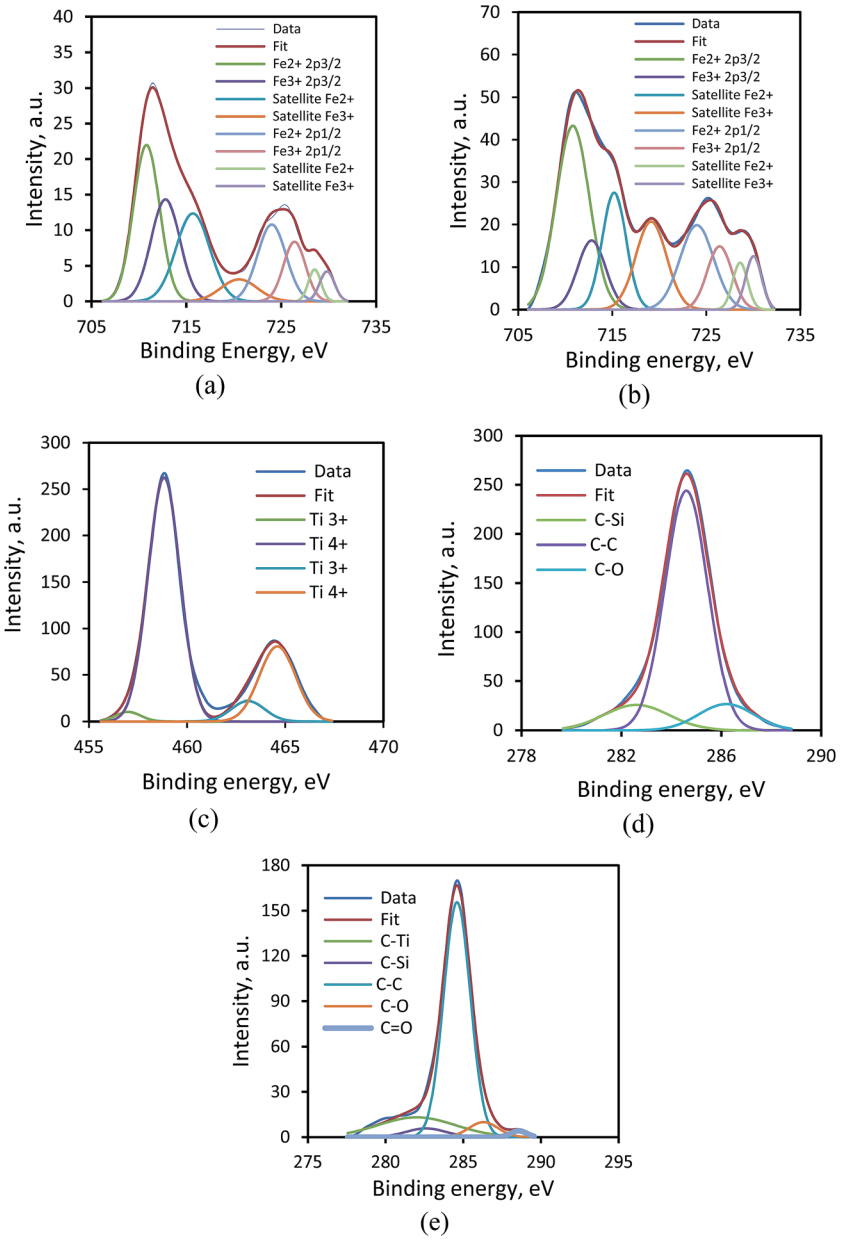

Fig. 3 XPS peak analysis of (a) Fe 2p peak on surface of Fe_3O_4 and (b) Fe_3O_4@TiO_2, (c) Ti 2p peak on surface of Fe_3O_4@TiO_2, and (d) C 1s peak on surface of Fe_3O_4 and (e) Fe_3O_4@TiO_2.

TiO_2 (Ti^{4+}) oxide layer on Fe_3O_4@TiO_2 is more obvious than Ti_2O_3 (Ti^{3+}), which indicates Ti^{4+} is in tetrahedral coordination with oxygen (TiO_2). High-resolution spectra analysis reveals that the oxidation content of Ti^{4+} on the surface was about 90%. The separation energy of the XPS peaks (ΔE) was found to be 5.8 eV, which is proportional to the spin orbit coupling constant. The present study is in agreement with previous findings.[29]

The XPS spectra of C 1s binding energy region for the Fe_3O_4 and Fe_3O_4@TiO_2 samples are shown in Fig. 3d and e. The surface chemical composition in the samples showed that the carbon adsorption reveals as a strong C–C bond (284.8 eV) and two weak C–Si (282.6 eV) and C=O (288.4 eV) peaks. In Fig. 3d, the peaks of C–Ti, C–Si, C–C, C–O and C=O are centered at 282, 282.6, 284.6, 286.3 and 288.6 eV, respectively. The shifting of the binding energy values to slightly negative shift and positive shift can be attributed to the oxidation of Fe_3O_4. These results reveal that TiO_2 and Fe_3O_4 present mostly as separate phases in the Fe_3O_4@TiO_2 nanoparticle photocatalyst, which is in agreement with the previous study.[30]

3.1.3. FT-IR analysis. The Fe_3O_4@TiO_2 photocatalyst was also analyzed by FTIR in order to verify the presence of magnetic recovered by TiO_2 (Fig. 4). The absorption peaks in the range of 1200 and 1460 cm^{-1} are attributed to methyl and methylene groups bending, wagging, scissoring, rocking and twisting vibrations. An absorption band associated with –C–H bond symmetric stretching are located at 2919 cm^{-1} and an asymmetric stretching vibration at about 2850 cm^{-1}. However, the absorption peak at 1698 cm^{-1} is attributed to the presence of

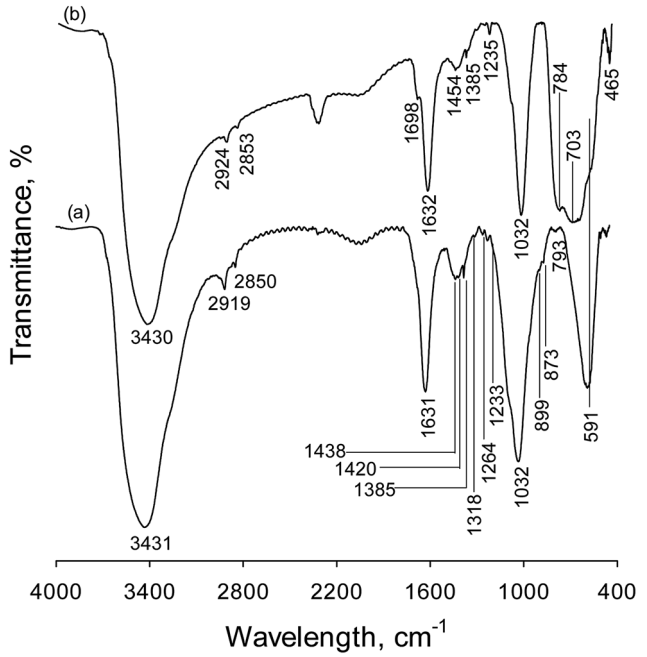

Fig. 4 FT-IR spectra of (a) Fe_3O_4 and (b) Fe_3O_4@TiO_2.

C═O stretching vibration. These peaks belong to the acetate and ethyl alcohol that were used as the solvent in photocatalyst preparation. The absorbance peak centered at 1032 cm^{-1} is attributed to a stretching vibration of C–O– functional group, with a shoulder peak at about 1090 cm^{-1} corresponded to the Si–O– stretching vibration of the SiO_2 layer in samples. In contrast to the FTIR spectra of Fe_3O_4, aforementioned peak intensities decrease in the spectrum of Fe_3O_4@TiO_2, indicating that the TiO_2 nanoparticles is coated well on the surface of the Fe_3O_4 nanospheres. In spectrum shown in Fig. 4a, the absorption peaks in 1632 and 3431 cm^{-1} are attributed to H–O–H bending and O–H stretching vibrations, respectively, of the free water molecules and adsorbed water on the sample surface. The FT-IR spectra of Fe_3O_4 show the characteristic band of magnetite, at 591 cm^{-1}, which is assigned to the stretching vibration of the Fe–O functional group and remained in a fixed position in the magnetite lattice, as indicated by the vertical inspection line in Fig. 4. There is a clear difference in the FT-IR spectra of Fe_3O_4 and Fe_3O_4@TiO_2. In Fe_3O_4@TiO_2 sample (Fig. 4b), the magnetite peak overlaps with broad bands of the stretching mode of Ti–O–Ti group, confirming the presence of TiO_2 layer. In addition, the peaks observed at 703 and 784 cm^{-1} in spectrum in Fig. 4b are due to the Ti–O–Ti stretching vibration of the anatase phase of TiO_2 layer. Also, XPS results confirm the formation of titanium oxide. In Fig. 4b, there is an O–H bond at 3431 cm^{-1} and a Ti–O stretch at 4650 cm^{-1} that are due to the stretching vibration of OH adsorbed on the surface (TiOH species) of nanoparticle and also a peak at 1631 cm^{-1} due to the bending vibrations of adsorbed water.

3.1.4. TEM and SEM analysis. Fig. 5 shows TEM and SEM images of Fe_3O_4 and Fe_3O_4@TiO_2 nanoparticles. Fig. 5a demonstrates that TEM images of Fe_3O_4 crystallites are ultrafine and the diameter of the aggregated particle size is of around 40 to 80 nm. Fig. 5b represents TEM image of a single core Fe_3O_4 nanoparticle with a size of about 80 nm. Fig. 3b shows that the Fe_3O_4 spherical shapes are compose of primary nanoparticles with a size of about 20 nm, which was comparable with the crystallite size of 15.64 nm in nanocrystalline bulk materials computed from the XRD pattern by using the Scherrer equation. Fig. 5c shows that the spherical shape of magnetite connects tightly to one another to form a sphere. According to Fig. 5d, the representative TEM image of a single core–shell Fe_3O_4@TiO_2 nanoparticle with well-defined core–shell structure and with an average size of 80 nm and the average thickness of the shell is 15 nm. The dark and bright regions correspond to the Fe_3O_4 and the shell, respectively. This phenomenon can be due to their different electron-absorbing abilities, *i.e.*, the electron binding ability of Fe_3O_4 is higher than that of non magnetic TiO_2. Therefore, the cores can be identified as the darker region compared to the shell area.[31,32] From the TEM images, it can be seen that a uniform shell of TiO_2 with a nanoscale thickness is coated on the Fe_3O_4 surface to form a core–shell structure. On the other hand, Fig. 5d represents more closely that the spherical-like core–shell nanoparticles are formed onto the Fe_3O_4 nanoparticle core and an anatase TiO_2 nanolayer shell. Fig. 5e demonstrates SEM image of the spherical morphology of core–shell nanoparticles with some degree of agglomeration. From the particle size distribution obtained from SEM image, it is possible to identify particles with different size, ranging from small particles to particles with up to 100 nm; nevertheless, the particle sizes estimated from the SEM were in the range of 30 to 100 mm. Fig. 5f confirms the element composition by SEM with energy dispersive X-ray (EDX) spectroscopy analysis. Fig. 5g EDX peaks taken from the core–shell Fe_3O_4@TiO_2 nanoparticle and spectra show strong Fe, Ti and O signals, which further confirms the formation of core–shell Fe_3O_4@TiO_2 nanoparticles. Si peak was attributed to the EAF dust used as the Fe source and remained on the sample during photocatalyst preparation, as XPS results also confirm the presence of Si on the Fe_3O_4@TiO_2 nanoparticles.

3.1.5. Magnetic characteristics. The magnetic property of as-synthesized Fe_3O_4 and Fe_3O_4@TiO_2 nanoparticles were studied by a vibrating sample magnetometer (VSM) at room temperature. The magnetic hysteresis loop measured at 300 K is shown in Fig. 6. The magnetization–hysteresis curves show that both Fe_3O_4 nanoparticles and Fe_3O_4@TiO_2 catalyst are magnetic and Fe_3O_4 have a magnetization saturation value of 25.66 emu g^{-1} while that of Fe_3O_4@TiO_2 catalyst is 6.64 emu g^{-1}. The reduction of saturation magnetization is prevalently associated with the existence of nonmagnetic TiO_2 shells on the surface of Fe_3O_4 as shown in Fig. 6. This result also indicates that the Fe_3O_4@TiO_2 nanocomposite remains magnetic after coating.[33] Due to the magnetic core–shell nanocomposite, the as-synthesized photocatalyst can be easily collected from aqueous solution by external magnetic field over a short period of time and then can be readily re-dispersed by slightly shaking it. The inset Fig. 6 shows the images obtained for dispersed aqueous solution (top inset) and separated from aqueous solution (down inset) by an external magnetic field. The

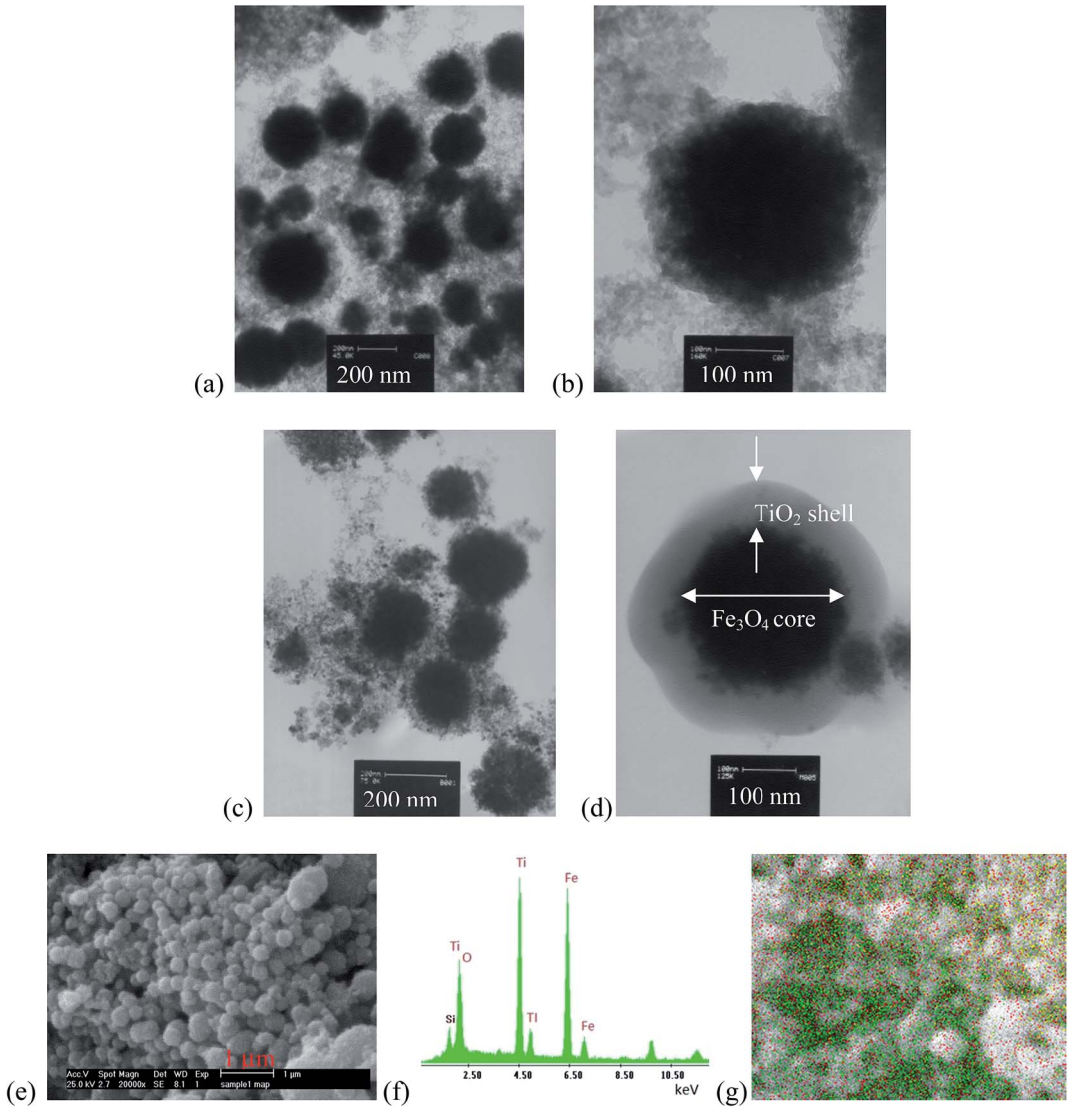

Fig. 5 TEM micrographs of (a) Fe_3O_4 nanoparticles, (b) single core of Fe_3O_4 nanoparticles (c) Fe_3O_4@TiO_2 nanoparticles, (d) and single core–shell of Fe_3O_4@TiO_2 (e) SEM, (f) EDX spectra of Fe_3O_4@TiO_2 core–shell and (g) EDX point image taken from core–shell Fe_3O_4@TiO_2 nanoparticle marked in the SEM images.

nanoparticles exhibited well magnetic behavior when they were magnetically separated from supernatant portion and redispersed in aqueous solution, suggesting the high potential sensitivity of as-synthesized magnetic photocatalyst.

3.2. Photocatalytic degradation

3.2.1. Effect of different photocatalyst. Fig. 7 shows the dark condition and adsorption under UV irradiation and the influence of five different photocatalysts (anatase TiO_2 and FT0.25, FT0.5, FT1 and FT2) on the decomposition kinetics and removal of organic compound of steel mill wastewater. Fig. 7a shows that the COD concentration diminishes exponentially with increasing time in the presence of Fe_3O_4@TiO_2 under UV irradiation. The apparent rate constant (k_{app}) verifies the shape of exponential decrease. Under a dark condition, the rate of COD removal was found to be much lower than the case of UV irradiation. The experimental data showed that the amount of COD adsorbed on the photocatalyst surface under a dark condition was found to be about 2.3% after 30 min (Fig. 7b), indicating a very low portion of the surface area of photocatalyst is accessible to COD adsorption. This means that the stereochemical structural limitations and its co-adsorbed with water molecules on the surface of photocatalyst are predominant for the reason that the water molecules are more abundant than COD molecules. At this operating condition, the rate constant of Fe_3O_4@TiO_2 at pH 3 after 30 min was calculated as 0.00067 min^{-1}. Hence, the COD removal of Fe_3O_4 magnetic nanoparticles under the UV light was about 7.7% after 30 min. The corresponding rate constant was calculated to be 0.00082 min^{-1}. From Fig. 7b, the results of our study showed that about 88.84% of the COD removal achieved in the presence of as-synthesized anatase TiO_2 under UV light after 90 min. At this operating condition, the corresponding apparent rate constant was 0.024 min^{-1}. The decomposition and mineralization of

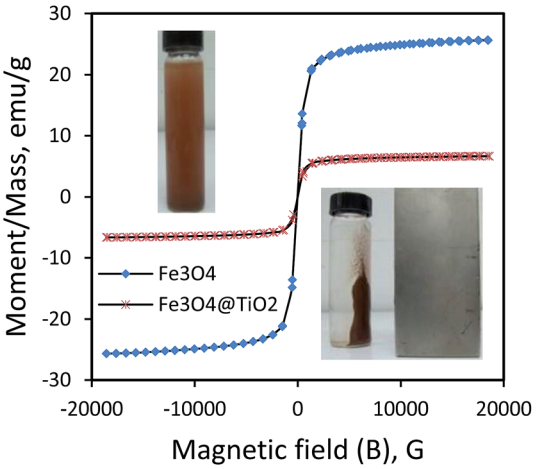

Fig. 6 Magnetization curves of Fe_3O_4 and Fe_3O_4@TiO_2 nanoparticles synthesized with molar ratio of 1 : 1 of Fe_3O_4 to TiO_2 (FT1).

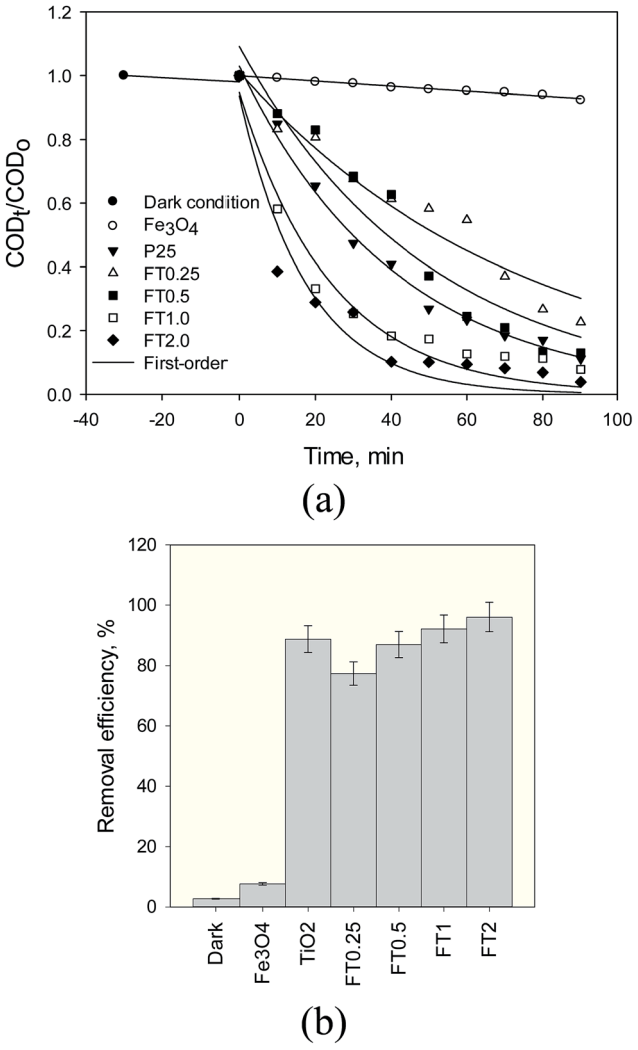

Fig. 7 Degradation kinetic curves of organic compounds of SMW using anatase TiO_2 and Fe_3O_4@TiO_2 with different TiO_2 loading (1 g L^{-1} photocatalyst dose, 1070 mg L^{-1} initial COD, pH 3, 90 min reaction time and 25 °C).

COD of steel mill wastewater enhanced more quickly and strongly in the presence of Fe_3O_4@TiO_2 under UV light in comparison with anatase TiO_2 photocatalysts. Fig. 7a also depicts the effect of adding TiO_2 onto Fe_3O_4 nanoparticles on the photocatalytic degradation kinetics of organic pollutants of wastewater. There was an improvement of COD removal efficiency with an increase in TiO_2 coated onto Fe_3O_4 surface to form nanocomposite of FT0.25, FT0.5, FT1 and FT2. In addition, our results showed when the ratio of Fe_3O_4 to TiO_2 increased, the photocatalytic degradation of the nanocomposite improved. This can be attributed to the large specific surface area and the more effective electron/hole pair separation. Wang *et al.*[24] have reported that the photocatalytic activity increased as the TiO_2 loading increased. The maximum COD removal efficiencies of 77.37, 87, 92.19 and 96.12% were obtained for FT0.25, FT0.5, FT1 and FT2 at a photocatalyst dose of 1 g L^{-1} after 90 min (Fig. 7b) and the corresponding rate constant was found to be 0.013, 0.020, 0.041 and 0.057 min^{-1}. It is clear that the rate constant of degradation reaction is influenced by the amount of TiO_2 coating onto Fe_3O_4, demonstrating the decomposition with the largest rate constant is the fastest. Fig. 8 compares photograph images of Fe_3O_4@TiO_2 nanocomposite with various TiO_2 loading onto magnetic Fe_3O_4 in the aqueous solution. First, the magnetic nanoparticles were suspended in aqueous solution and were then applied to an external magnetic field. Fig. 8 shows that FT0.25, FT0.5 and FT1 samples separated completely from the aqueous solution, and there were no signs of suspension of the nanoparticles in the test beakers. However, the magnetic nanoparticles coated with TiO_2 with a ratio of 2 : 1 onto Fe_3O_4, namely FT2, were not well separated from aqueous by external magnet, indicating some TiO_2 particles have failed to coat on the magnetic core. For the photocatalytic activity of Fe_3O_4@TiO_2 nanoparticles with four ratios of coating, we chose the one that has the biggest rate constant. In the case of the suspension of FT2, since sediments of Fe_3O_4@TiO_2 nanoparticles became visible throughout the test beakers after 30 min and resuspending the aqueous solution, most of the Fe_3O_4@TiO_2 nanoparticles were still suspended in the water (Fig. 8b). Therefore, with the comparison between the obtained results of the apparent degradation rate of the photocatalytic reaction of Fe_3O_4@TiO_2 nanocomposite and the clear solution of photograph of FT1 (Fig. 8c), it is obvious that FT1 should be chosen as optimum photocatalyst, that can be used to obtain the apparent rate constants of other experimental conditions.

3.2.2. Effect of pH. The pH of the solution is a major factor affecting the photocatalytic activity, because it dedicates the surface charge of the photocatalyst and the size of aggregates it forms.[34] It can be explained that the solution pH positively correlates with their photocatalytic performance, indicating that the organic wastewater compounds are to be differences in hydrophobicity, solubility and speciation behaviors. When a pH of a solution decreases below its pK_a value, an organic compound exists in a neutral form and it transfers from neutral to a negatively charged when the solution pH increases above its pK_a value. Accordingly, organic pollutants decomposition rate of photocatalytic reaction was increased significantly with

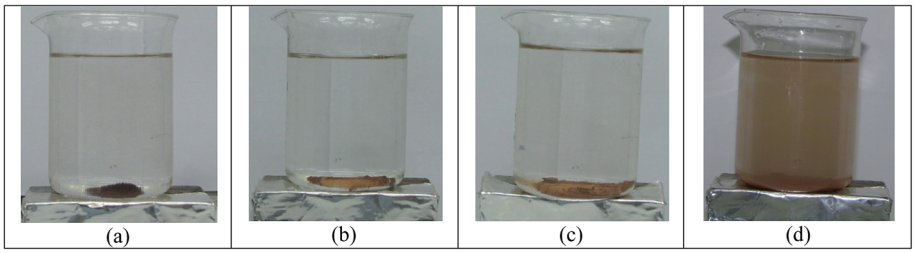

Fig. 8 Photograph comparing appearance of aqueous of magnetic nanoparticles coated with TiO_2. (a) FT0.25, (b) FT0.5, (c) FT1, and (d) FT2 suspensions after 30 min.

increasing pH. The acidic solution favors degradation of organic compound onto TiO_2 surface. Thus, degradation efficiency increased. At this pH, there is also formation of $OH^{\bullet}$ radicals, which react with organic molecules and increase the degradation level. This means that $OH^{\bullet}$ radicals are formed on the surface of Fe_3O_4@TiO_2 by the reaction of gaps in the valence band (h_{vb}^{+}) with adsorbed water molecules or hydroxide of surface titanol groups (TiOH). Furthermore, photogenerated electrons react with oxygen molecules to produce superoxide ($O_2^{-\bullet}$). This $O_2^{-\bullet}$ can react with protons and O_2 to produce hydroperoxyl radicals ($HO_2^{\bullet}$). The formation of hydrogen peroxide (H_2O_2) can occur either by water oxidation (by holes) or by two conduction band electron reduction of the adsorbed water. Aforementioned processes are represented by the following equations:

$$TiO_2 + h\nu \rightarrow e_{cb}^{-} + h_{vb}^{+} + \text{heat} \quad (14)$$

$$h_{vb}^{+} + H_2O \rightarrow OH^{\bullet} + H^{+} \quad (15)$$

$$e_{cb}^{-} + O_2 \rightarrow O_2^{-\bullet} \quad (16)$$

$$e_{cb}^{-} + O_2 + H^{+} \rightarrow HO_2^{\bullet} \quad (17)$$

$$HO_2^{\bullet} \rightarrow O_2^{-\bullet} + H^{+} \quad (18)$$

$$e_{cb}^{-} + HO_2^{\bullet} + H^{+} \rightarrow H_2O_2 \quad (19)$$

In addition, $OH^{\bullet}$ radicals can be produced by cleavage of H_2O_2 by one of the following reactions:

$$H_2O_2 + h\nu \rightarrow 2HO^{\bullet} \quad (20)$$

$$H_2O_2 + O_2^{-\bullet} \rightarrow HO^{\bullet} + O_2 + HO^{-} \quad (21)$$

$$e_{cb}^{-} + H_2O_2 \rightarrow HO^{\bullet} + HO^{-} \quad (22)$$

Finally, oxidation of organic compounds to CO_2 mineralization occurs in a solution saturated with activated oxygen species ($O_2^{-\bullet}$, $HO_2^{\bullet}$, H_2O_2, $OH^{\bullet}$), which may affect the yield of oxidation.

The experiments were carried out at pH 3, 4, 5, 6, 7, and 8 for 90 min reaction time (Fig. 9). Fig. 9a shows that anchored in the results of our experiments, decomposition of organic pollutants using Fe_3O_4@TiO_2 photocatalyst for steel mill wastewater follows the first-order kinetic. This figure shows that the decomposition rate of the organic compounds decreased with increasing pH of the solution. The plot of COD_t/COD_o *versus* reaction time gives a good relationship ($R^2 > 0.99$), which is supportive of the good agreement of fitting the reaction data in first-order kinetic and the apparent reaction rate constant of the photocatalytic decomposition at pH 3, pH 4, pH 5, pH 6, pH 7 and pH 8 were calculated as 0.043, 0.038, 0.036, 0.035, 0.034 and 0.030 min^{-1}, respectively. As the pH of the solution is increased, the degradation of organic molecules onto catalyst surface decreased. Therefore, degradation rate constants were observed to be low at basic pH condition. Fig. 9b shows that neutral pH and moderate acidic pH conditions were appropriate for organic degradation of steel mill wastewater by Fe_3O_4@TiO_2. Fig. 9b shows that the maximum degradation of about 94% was observed at pH 3. This phenomenon could be led to obvious justification that degradation of organic compounds exhibited different behaviors with strong pH dependence of the solution.[35,36] To explain, electrostatic interactions and pH-dependent trend between the protonated surface of photocatalyst ($TiOH_2^{+}$) and cations of organic compound of COD results to strong adsorption and subsequent efficient decomposition of organic pollutants:

$$\text{pH} < \text{pzc TiOH} + H^{+} \rightarrow TiOH_2^{+} \quad (23)$$

The existing form of organic compounds and surface charges of Fe_3O_4@TiO_2 is also related to solution pH. Fig. 9c shows that the point of zero charge (pzc) for anatase TiO_2 used in this study was around pH = 4.1. Therefore, catalyst surface is positive in solution at moderate acidic (pH < 4.1) and negatively at basic condition.[37] Repulsions between same charged Fe_3O_4@TiO_2 surfaces prevent the agglomeration of the catalyst. Similar observations on the effect of pH for TiO_2 photocatalyst have been reported in photocatalytic decomposition of COD of some other pollutants.[37,38] At pH 8, TiO_2 particle surfaces should mainly be neutral. Minimum degradation of 85.24% was observed at pH 8 (Fig. 9b). To explain, basic pH electrostatic interactions between deprotonated surface of photocatalyst (TiO^{-}) and organic compound of COD leads to adsorption and degradation of organic compounds:

$$\text{pH} > \text{pzc TiOH} + OH^{-} \rightarrow TiO^{-} + H_2O \quad (24)$$

However, the band hole position may be moved to more negative value with increasing pH, causing in a reduction of oxidation potentials. Consequently, the solution pH at

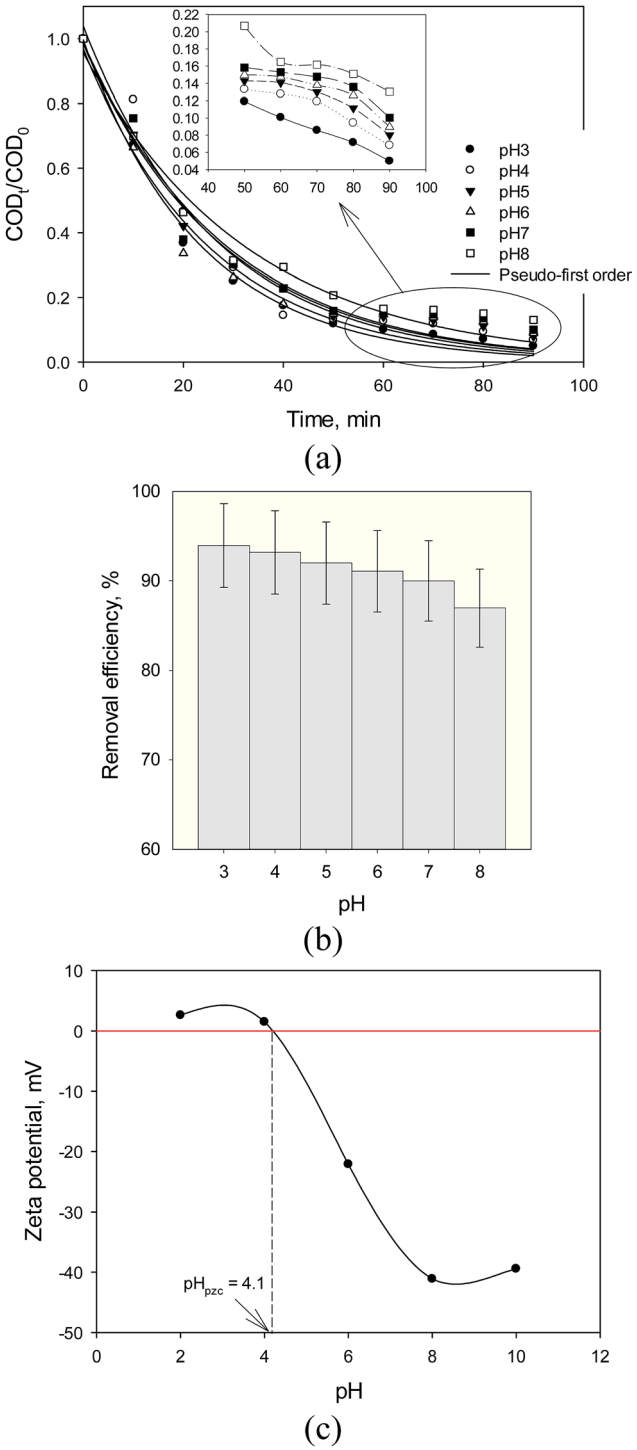

Fig. 9 (a) Kinetic curves, (b) removal efficiency of SMW with Fe_3O_4@TiO_2 (FT1) at different pH (1 g L^{-1} photocatalyst dosage, 920 mg L^{-1} initial COD, 90 min reaction time and 30 °C) and (c) zeta potential and the pzc of Fe_3O_4@TiO_2.

a suitable value, due to electrostatic attraction, would influence the degradation of organic compound of COD in wastewater and the adsorption on the surface of Fe_3O_4@TiO_2 photocatalyst and thus it is found to favor efficient degradation rate of organic compounds.

3.2.3. Effect of dose of photocatalyst. For economic consideration and the penetration depth of light irradiation by the high turbidity suspension and light shadowing effects at high dose of photocatalyst, experiments were performed to optimize the dose of the Fe_3O_4@TiO_2 photocatalyst in order to maximize the density of surface active sites and reactivity for the photocatalytic mineralization of organic pollutants. This part of the experiment was carried out under the following conditions: catalyst dose of 0.25, 0.5, 1 and 2 g L^{-1}, initial COD 860 mg L^{-1}, pH 7, temperature of 30 °C, and 90 min reaction time. Fig. 10a depicts a good agreement of the nonlinear relationship of photodegradation kinetics with experimental data (R^2 > 0.97) and the apparent rate constants of the photocatalytic degradation at 0.25, 0.5, 1 and 2 were calculated as 0.007, 0.033, 0.043 and 0.058 min^{-1}, respectively. The variations in COD removal efficiency obtained are illustrated in Fig. 10b. Correspondingly,

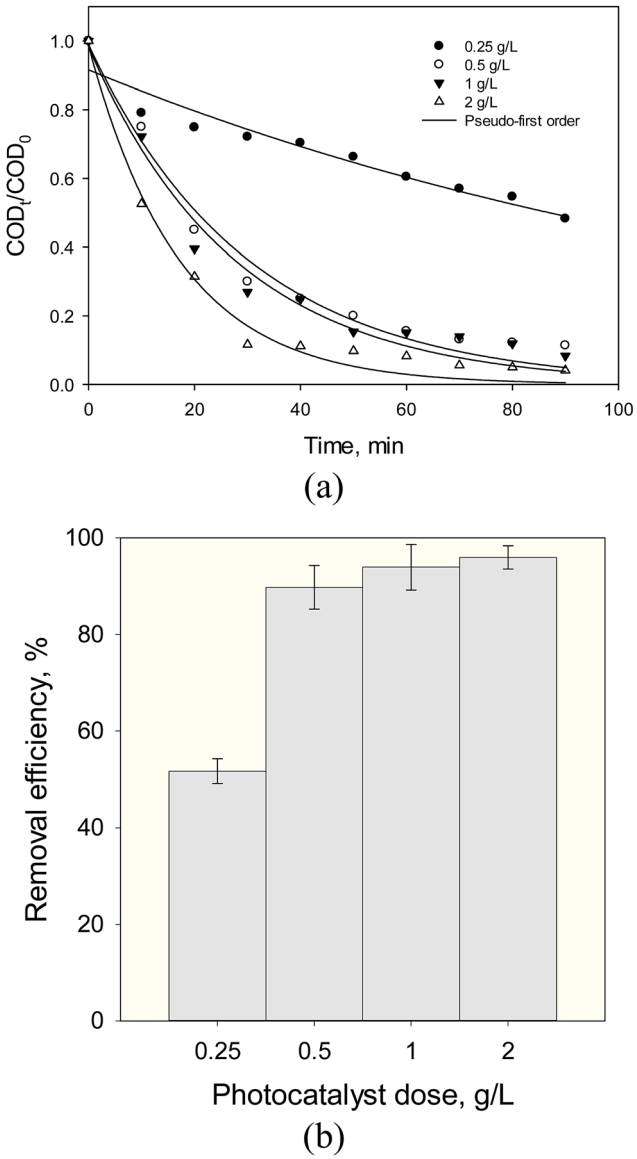

Fig. 10 (a) Kinetic curves, (b) removal efficiency of SMW with Fe_3O_4@TiO_2 (FT1) at different photocatalyst dose (pH = 3, 920 mg L^{-1} initial COD, 90 min reaction time and 30 °C).

when the photocatalyst dose was increased from 0.25 g to 2 g, the COD removal efficiency was improved from 51.74 to 95.93%. It was speculated that excessive amount of the Fe_3O_4@TiO_2 photocatalyst added to the solution has significant efficiency of photodegradation under UV radiation. However, a further increase in photocatalyst dose above the optimum level (up to 3 g L^{-1}) led to irregular light intensity scattering, so that the reaction rate was lower with an increase in catalyst dosage (figure not shown). Our results showed that the decomposition rate of COD increases linearly with catalyst dose up to 2 g L^{-1} and then decreases due to increase in solution turbidity.

3.2.4. Effect of reaction temperature. Fig. 11 shows the temperature effect on the COD degradation in the experiments at different temperature in the range of 30–55 °C, whereas the initial COD concentration, dose of photocatalyst, pH and contact time were fixed at 1070 mg L^{-1}, 1 g L^{-1}, 3 and 90 min reaction time, respectively. Based on the experimental results, degradation of organic compounds in wastewater using heterogeneous Fe_3O_4@TiO_2 catalysts follows pseudo apparent first-order kinetics (Fig. 11a). Over the examined range temperature, COD degradation was increased as the temperature rose (Fig. 11b). The maximum removal efficiency was obtained at a temperature of 55 °C. Fig. 11c illustrates that the Arrhenius equation demonstrates the effect of a change of temperature on the rate constant from 15 to 45 °C. The calculated E_a obtained for the photodegradation of organic pollutants in steel industry wastewater by heterogeneous Fe_3O_4@TiO_2 and the corresponding frequency factor and R^2 are presented in Table 3. This is to be stated that the activation energy of Fe_3O_4@TiO_2 system is relatively less than the other reported in the literatures.[21] Fig. 11d shows the Eyring plot of SMW with Fe_3O_4@TiO_2 at different temperature and Table 3 provides results of the computations of Arrhenius and TST theories for heterogeneous photocatalytic decomposition of COD of steel mill wastewater using Fe_3O_4@TiO_2 nanoparticles. The values of both $\Delta^{\ddagger}H^{o}$ and $\Delta^{\ddagger}G^{o}$ were found to be positive, while that of $\Delta^{\ddagger}S^{o}$ was negative. The increasing value of k_{app} and the positive values of $\Delta^{\ddagger}H^{o}$ with increasing temperature prove that the decomposition of COD using the Fe_3O_4@TiO_2 is an endothermic process.[21] The endothermic nature of photocatalytic process is possibly due to the electrostatic interaction between the hydrophobic character of TiO_2 on the photocatalyst surface and organic pollutants. The hydrophobic surface property of Fe_3O_4@TiO_2 photocatalyst favors adsorption of organic pollutants onto charged TiO_2 surface to achieve efficient photocatalytic degradation and decreases agglomerations of Fe_3O_4@TiO_2 nanoparticles. In addition, the positive values of $\Delta^{\ddagger}G^{o}$ increased with an increase in experimental temperature. At a given temperature the more positive value of $\Delta^{\ddagger}G^{o}$ at the higher temperature demonstrates that the system will go in the direction of producing reactants (nonspontaneous process) and poor adsorption tendency of organic pollutants on Fe_3O_4@TiO_2 or undesired photocatalytic degradations under given experimental temperatures. Finally, the negative value of standard entropy change of activation ($\Delta^{\ddagger}S^{o}$) indicates that interactions of potential-determining ions with the active surface sites (H^+/OH^- ions and TiO_2) are less hydrated at the solid/liquid interface.

3.3. Studies upon photocatalyst recycling

To examine the reusability and photocatalytic stability of Fe_3O_4@TiO_2 nanocomposite, recycling experiments were also

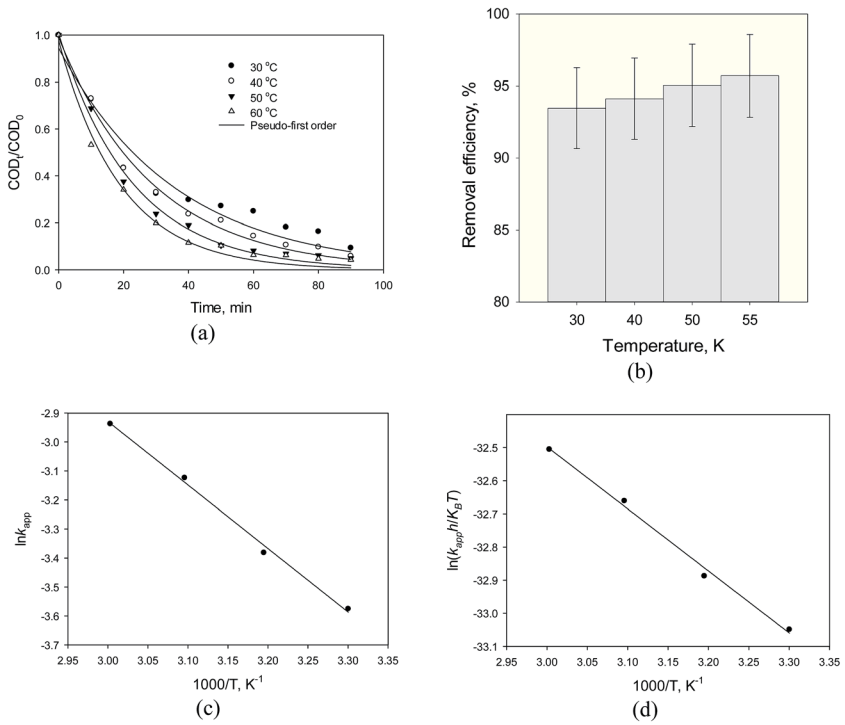

Fig. 11 (a) Kinetic curves, (b) removal efficiency, (c) the Arrhenius plot and (d) the Eyring plot of SMW with Fe_3O_4@TiO_2 (FT1) at different temperature (photocatalyst dose 1 g L^{-1}, pH = 3, 920 mg L^{-1} initial COD, and 90 min reaction time).

Table 3 Kinetic and activation parameters for the photocatalytic degradation of organic pollutants in petroleum refinery wastewater[a]

			Arrhenius theory			Transition state theory					
T, K	k_{app}, min^{-1}	$\ln(k_{app}h/K_BT)$	E_a, kJ mol^{-1}	A, min^{-1}	R^2	$\Delta^{\ddagger}H^o$, kJ mol^{-1}	$\Delta^{\ddagger}S^o$, kJ K^{-1} mol^{-1}	$\Delta^{\ddagger}G^o$, kJ mol^{-1}	A, min^{-1}	$E_a{}^a$, kJ mol^{-1}	R^2
303	0.028	−37.14	18.21	38.21	0.9957	15.57	−0.258	93.60	13.41	18.09	0.9942
313	0.034	−36.98						96.17	13.85	18.18	
323	0.044	−36.76						98.75	14.30	18.26	
325	0.053	−36.60						101.32	14.74	18.34	

[a] $E_a = \Delta^{\ddagger}H^o + RT$.

conducted under optimal conditions. At the end of the first step of decomposition reaction cycle, the Fe_3O_4@TiO_2 nanoparticles were separated from aqueous solution by external magnetic field for a period of 90 min and then the treated wastewater was discharged. The separated photocatalyst was then reused without any treatment. The advantage of the magnetic photocatalytic process of organic pollutant degradation is to be employed for a number of working cycles in order to maintain low cost and the good photocatalytic activity, the easy separation from the aqueous solution, the possibility of reuse. To test the possibility of reusing the photocatalyst Fe_3O_4@TiO_2, the experiments were immersed in steel industry wastewater at pH 3, a photocatalyst dose of 1 g L^{-1} and 55 °C under exposure to ultraviolet radiation. Under these conditions, the degradation removal efficiency of the photocatalyst was obtained more than 95% within 90 min. When the organic pollutants were degraded, Fe_3O_4@TiO_2 photocatalyst were reused for further wastewater immersion for COD degradation measurement. The results showed that Fe_3O_4@TiO_2 nanoparticles by two and three cycles could degrade organic pollutant of wastewater by slight decreases in the COD removal of 0.90 and 1.40, respectively. The decrease in the removal efficiency of photocatalytic decomposition in the third cycle of the experiment was about 2.28% and 2.75 and 3.16% after the 4 and 5 cycles, respectively. This means that after the photocatalyst Fe_3O_4@TiO_2 was reused in five successive cycles, the degradation removal efficiency of wastewater of 92.54% was obtained, indicating its photocatalytic activity. Our results have demonstrated that the Fe_3O_4@TiO_2 photocatalyst offers great potential photocatalytic activity with a highly efficient degradation rate to be stable and reusable after several treatment cycles with a lower number of possible recycling cycles.

3.4. Comparison of Fe_3O_4@TiO_2 with other photocatalyst

The comparison of maximum percentage removal of as-synthesized Fe_3O_4@TiO_2 photocatalyst by various photocatalyst with respect to different solution pH, different type of photocatalyst, photocatalyst dose and temperature was judged from the literatures. A study demonstrated that the reason for the variations in the photocatalytic activity of TiO_2–SiO_2 composite are probably related on the effect of change in the molar ratio of Ti to Si.[39] The degradation efficiency of RhB under visible light after 40 min irradiation was about 98.6%, while that of pure TiO_2 was only 11.9%. They have stated that the superoxide radicals and photogenerated holes are the key reactive species for the decomposition of RhB. Chládková *et al.*[40] have investigated the effect of pH (3–10) on the decomposition of Reactive Red 195 using a mixture of amorphous hydrated TiO_2 and crystalline TiO_2. They stated that the degradation adsorption of RR195 was increased at the acidic pH compared to the alkaline pH, which was attributed to the strong electrostatic interaction between the catalyst surface and the dye molecules at lower pH values. Under the conditions tested, the degradation efficiency was reported to be at 76 and 66% for pH 3 and 10, respectively. A study[20] has shown that the percentage decomposition of photocatalyst increases with increasing photocatalyst dose and then decreases at high dose because of a decrease of light scattering and screening effects among photocatalyst particles. They reported that a maximum reduction of 80% COD for petroleum refinery wastewater using TiO_2/Fe-ZSM-5 at pH of 4, a photocatalyst concentration of 2.1 g L^{-1}, a temperature of 45 °C and UV exposure time of 240 min. In addition, the problem of particle agglomeration (particle–particle interactions) also increases at high dose of photocatalyst may result in the degradation efficiency of photocatalyst. Zhang *et al.*[41] compared the photocatalytic degradation of gaseous 1,2-dichlorobenzene (*o*-DCB) using $ZnFe_2O_4$/In_2O_3 hybrid nanoheterostructures under visible light. After 8 h irradiation, the degradation efficiencies of In_2O_3, $ZnFe_2O_4$ and $ZnFe_2O_4$/In_2O_3 were reported to be 41.8, 56.7 and 68.7%, respectively. A possible reason stated was that the strong interaction formed at the intimate interfaces between In_2O_3 and $ZnFe_2O_4$ is the favorite for the migration and separation of charge carriers, resulting in long lived e/h^+ pairs. It was found that effect of temperature on biodiesel (90% soybean oil and 10% lard) oxidation was evaluated by kinetic and thermodynamic data using sodium methoxide as catalyst.[42] However, few researches have studied temperature influence on photocatalytic degradation activity.[21] The kinetic parameters were calculated by the L–H model and the energy of activation for decomposition of COD in petroleum refinery wastewater obtained by Arrhenius equation which was reported at about 18.76 kJ mol^{-1}. The thermodynamic activation parameters of the reactions, evaluated by the Eyring equation based on the TST, indicated nonspontaneous processes with a $\Delta^{\ddagger}G^o$ value of 92.82 kJ mol^{-1}, a $\Delta^{\ddagger}H^o$ value of 16.26 kJ mol^{-1} and a $\Delta^{\ddagger}S^o$ value of −0.266 kJ K^{-1} mol^{-1} at optimum pH of 4, TiO_2/Fe-ZSM-5 dose of

3 g L^{-1} and 45 °C. The heterogeneous photocatalytic decomposition of phenol in aqueous solution was studied using TiO_2 photocatalyst under UV light irradiation in an annular type photoreactor.[43] The kinetic parameters were modelled by the L–H model and the apparent reaction rate constant and removal efficiency for phenol degradation corresponding to the flow rate of 10 L h^{-1} and 0.4 g L^{-1} TiO_2 dose was found to be 0.00288 min^{-1} and 36%, respectively. Abbasi and *et al.*[44] synthesized Fe_2O_3 nanoparticles *via* a microwave method and Fe_2O_3–TiO_2 nanocomposites by a sonochemical-assisted procedure. Under UV light irradiation, the photocatalytic activity of Fe_2O_3–TiO_2 nanocomposites was assessed by measuring the decomposition of MB in aqueous media. The maximum degradation efficiency of MB was achieved about 81% after 100 min synthesis of carboxymethyl-β-cyclodextrin-functionalized Fe_3O_4@TiO_2 (CMCD-Fe_3O_4@TiO_2) core–shell nanoparticle was prepared for photocatalytic ability to degrade bisphenol A (BPA) and dibutyl phthalate (DBP) from aqueous solution.[45] They reported that the degradations of BPA and DBP in the presence of CMCD-Fe_3O_4@TiO_2 and Fe_3O_4@TiO_2 using a Hg vapor lamp were obtained to be complete for BPA within 60 min, whereas it was incomplete for DBP even after 180 min of illumination. They also studied the photocatalytic activity of the CMCD-Fe_3O_4@TiO_2 nanoparticles for multiple usages. It maintained 90% of efficiency after 10 cycles compared to the first use efficiency.

In summary, the catalytic mechanism of Fe_3O_4@TiO_2 nanocomposites in mineralization of organic compounds is known by the researchers in the field of environmental photocatalysis and especially they can easily be recycled and reused by external magnetic field due to their strong magnetic response. Moreover, our results demonstrated that the greater reactivity of the as-fabricated photocatalyst is more pronounced than for P25 TiO_2. However, Fe_3O_4 core and TiO_2 shell in the nanocomposite core–shell structure play a key role in the photocatalytic degradation process. The active sites on the surface of TiO_2 shell layer can act as adsorbent for photocatalytic function in mineralization of the organic compounds under UV light irradiation and the magnetite particle with about 25 nm crystalline Fe_3O_4 core allows for the magnetic separation function from the dispersion once yields CO_2 and water, *i.e.*, complete mineralization.

4. Conclusion

The experimental data of this study demonstrated that Fe_3O_4 nanoparticles were successfully synthesized by solvothermal reaction using EAF dust reaction substrate, sodium acetate as a reducer and ethylene glycol as solvent. The core–shell Fe_3O_4@TiO_2 nanocomposites were synthesized by the sol–gel method. The characterization results showed that samples presented a high degree of superparamagnetism and the particle size of Fe_3O_4 obtained was about 100 nm. The second major finding was that the photocatalytic activity for the decomposition of COD of steel mill wastewater was higher in the acidic pH. In addition, Fe_3O_4@TiO_2 nanoparticles can be reused several times without significant decrease of their efficiency of the oxidation process which indicates that they are suitable candidates for the practical use in the industrial wastewater treatment. Returning to the question posed at the beginning of this study, it is now possible to state that, using EAF dust is a good alternative to minimize the costs of preparation of photocatalyst, which is considered as an environmentally friendly method, because no salts are volatile or harmful that can be easily recycled. In other words, the Fe_3O_4 nanoparticles derived in this study could help to reduce the burden on the environment from EAF dust, increase the improvement of the source nanomaterial and reduce the cost of raw materials. Finally, the findings of this study have an important suggestion for future work that other metal oxide nanoparticles could be synthesized from the precursor reacting with HCl in aqueous solution by hydrothermal precipitation with NaOH.

Acknowledgements

The study was funded by a grant from the Iran National Science Foundation and the Ministry of Science and Technology, Iran, and the Tarbiat Modares University (TMU). The authors wish to thank Mrs Haghdoust for her assistance (Technical Assistant of Environmental Laboratory) and Tarbiat Modares University, Ministry of Science and National Science Foundation for their financial support.

References

1 G. Salihoglu, V. Pinarli, N. K. Salihoglu and G. Karaca, *J. Environ. Manage.*, 2007, **85**, 190–197.
2 T. Sofilić, A. Rastovčan-Mioč, Š. Cerjan-Stefanović, V. Novosel-Radović and M. Jenko, *J. Hazard. Mater.*, 2004, **109**, 59–70.
3 S. Smith, X. Zhou and C. Nassaralla, *Iron Steelmaker*, 2000, **27**, 69–76.
4 J. O. Edwards and R. Curci, in *Catalytic Oxidations with Hydrogen Peroxide as Oxidant*, Springer, 1992, pp. 97–151.
5 C. Huang, C. Dong and Z. Tang, *Waste Management*, 1993, **13**, 361–377.
6 O. Legrini, E. Oliveros and A. Braun, *Chem. Rev.*, 1993, **93**, 671–698.
7 W. H. Glaze, J.-W. Kang and D. H. Chapin, *Ozone: Sci. Eng.*, 1987, **9**, 335–352.
8 G. V. Buxton, C. L. Greenstock, W. P. Helman and A. B. Ross, *J. Phys. Chem. Ref. Data*, 1988, **17**, 513–886.
9 J. M. Herrmann, *Top. Catal.*, 2005, **34**, 49–65.
10 S. Malato, P. Fernández-Ibáñez, M. Maldonado, J. Blanco and W. Gernjak, *Catal. Today*, 2009, **147**, 1–59.
11 J. Blanco-Galvez, P. Fernández-Ibáñez and S. Malato-Rodríguez, *J. Sol. Energy Eng.*, 2007, **129**, 4–15.
12 R. J. Watts, S. Kong and W. Lee, *J. Environ. Eng.*, 1995, **121**, 730–735.
13 P. Fernández-Ibáñez, J. Blanco, S. Malato and F. De Las Nieves, *Water Res.*, 2003, **37**, 3180–3188.
14 V. Loddo, G. Marci, L. Palmisano and A. Sclafani, *Mater. Chem. Phys.*, 1998, **53**, 217–224.

15 S. Suresh and D. Ramesh Raja, *Int. J. Chem., Environ. Pharm. Res.*, 2011, **5**, 349–360.
16 S. Xuan, W. Jiang, X. Gong, Y. Hu and Z. Chen, *J. Phys. Chem. C*, 2009, **113**, 553–558.
17 T. Arai, T. Sato, H. Kanoh, K. Kaneko, K. Oguma and A. Yanagisawa, *Chem.–Eur. J.*, 2008, **14**, 882–885.
18 S. Xuan, W. Jiang, X. Gong, Y. Hu and Z. Chen, *J. Phys. Chem. C*, 2008, **113**, 553–558.
19 X. W. Lou and L. A. Archer, *Adv. Mater.*, 2008, **20**, 1853–1858.
20 Z. Ghasemi, H. Younesi and A. A. Zinatizadeh, *Chemosphere*, 2016, **159**, 552–564.
21 Z. Ghasemi, H. Younesi and A. A. Zinatizadeh, *J. Taiwan Inst. Chem. Eng.*, 2016, **65**, 357–366.
22 M. Shokouhimehr, Y. Piao, J. Kim, Y. Jang and T. Hyeon, *Angew. Chem.*, 2007, **119**, 7169–7173.
23 T. Xin, M. Ma, H. Zhang, J. Gu, S. Wang, M. Liu and Q. Zhang, *Appl. Surf. Sci.*, 2014, **288**, 51–59.
24 D. Wang, J. Yang, X. Li, J. Wang, H. Zhai, J. Lang and H. Song, *Phys. Status Solidi A*, 2017, **214**, 1600665.
25 J. Liu, Z. Sun, Y. Deng, Y. Zou, C. Li, X. Guo, L. Xiong, Y. Gao, F. Li and D. Zhao, *Angew. Chem., Int. Ed.*, 2009, **48**, 5875–5879.
26 APHA, *Standard Methods for the Examination of Water and Wastewater*, American Public Health Association, Washington, DC, 1998.
27 P. Atkins and J. de Paula, *Physical Chemistry*, W. H. Freeman, 2002.
28 F. Meng, W. Wei, X. Chen, X. Xu, M. Jiang, L. Jun, Y. Wang and Z. Zhou, *Phys. Chem. Chem. Phys.*, 2016, **18**, 2510–2516.
29 Y. Fu, H. Du, S. Zhang and W. Huang, *Mater. Sci. Eng., A*, 2005, **403**, 25–31.
30 X. Qiao, Y. Luo, A. Sun, C. Wang, J. Zhang, C. Chu, J. Guo and G. Xu, *RSC Adv.*, 2015, **5**, 6489–6493.
31 S. C. Xu, Y. Q. Yang, Y. S. Liu, H. Miao, M. Dong, J. Yang, J. M. Zhang, Z. Dai, G. Zheng and B. Sun, in *Advanced Materials Research*, Trans Tech Publ, 2011, pp. 216–219.
32 X. Shen, Y. X. Wang, L. Q. Lu, Y. L. Chen, Y. Xia and Y. H. Li, *J. Sol-Gel Sci. Technol.*, 2010, **54**, 340–346.
33 R. E. Dunin-Borkowski, M. R. McCartney, R. B. Frankel, D. A. Bazylinski, M. Pósfai and P. R. Buseck, *Science*, 1998, **282**, 1868–1870.
34 W. Bahnemann, M. Muneer and M. M. Haque, *Catal. Today*, 2007, **124**, 133–148.
35 D. Chen and A. K. Ray, *Water Res.*, 1998, **32**, 3223–3234.
36 S. Sakthivel, B. Neppolian, M. Shankar, B. Arabindoo, M. Palanichamy and V. Murugesan, *Sol. Energy Mater. Sol. Cells*, 2003, **77**, 65–82.
37 M. Vohra and K. Tanaka, *Environ. Sci. Technol.*, 2001, **35**, 411–415.
38 W. Z. Tang and H. An, *Chemosphere*, 1995, **31**, 4157–4170.
39 Z.-Y. Yang, G.-Y. Shen, Y.-P. He, X.-X. Liu and S.-J. Yang, *J. Porous Mater.*, 2016, **23**, 589–599.
40 B. Chládková, E. Evgenidou, L. Kvítek, A. Panáček, R. Zbořil, P. Kovář and D. Lambropoulou, *Environ. Sci. Pollut. Res.*, 2015, **22**, 16514–16524.
41 F. Zhang, X. Li, Q. Zhao and D. Zhang, *ACS Sustainable Chem. Eng.*, 2016, **4**, 4554–4562.
42 D. Borsato, D. Galvan, J. L. Pereira, J. R. Orives, K. G. Angilelli and R. L. Coppo, *J. Braz. Chem. Soc.*, 2014, **25**, 1984–1992.
43 R. Kar, O. Gupta, K. Mandol and S. Bhattacharjee, *J. Chem. Eng. Process Technol.*, 2013, **4**, 143.
44 A. Abbasi, D. Ghanbari, M. Salavati-Niasari and M. Hamadanian, *J. Mater. Sci.: Mater. Electron.*, 2016, **27**, 4800–4809.
45 R. Chalasani and S. Vasudevan, *ACS Nano*, 2013, **7**, 4093–4104.